


Cite this: *RSC Adv.*, 2019, 9, 9475Received 6th December 2018  
Accepted 12th March 2019

DOI: 10.1039/c8ra10041a

rsc.li/rsc-advances

# A facile method to synthesize $\text{CoV}_2\text{O}_6$ as a high-performance supercapacitor cathode†

Xinrui He,<sup>‡</sup> Jing Jiang,<sup>‡</sup> Hanqing Tian, Yi Niu, Zhipeng Li, Yalin Hu, Jiahao Fan and Chao Wang \*

Transition metal oxides can easily lose electrons and thus possess multiple accessible valences. Especially, if two different transition metals are combined, better capacity and cycling stability are achieved. In this study, a binary transition metal oxide,  $\text{CoV}_2\text{O}_6$ , was synthesized *via* a facile co-precipitation process for use as a supercapacitor cathode; the as-synthesized  $\text{CoV}_2\text{O}_6$  exhibited high-capacity ( $306.6 \text{ F g}^{-1}$ ,  $1 \text{ A g}^{-1}$  and  $219.2 \text{ F g}^{-1}$ ,  $20 \text{ A g}^{-1}$ ) and stable cycling stability, retaining 83.3% of its initial specific capacitance after 20 000 cycles. We believe that this facile synthesis process presents an effective method and a new opportunity for promoting the application of electrode materials based on binary transition metal oxides in supercapacitors.

## Introduction

The development of supercapacitor materials with high capacitance and cycling stability is of significant importance for next generation energy storage devices.<sup>1</sup> The type of electrode materials has been considered as a critical factor affecting the electrochemical performance of the supercapacitors; therefore, there is an urgent need for researchers to develop new electrode materials that are efficient, clean and sustainable.<sup>2–4</sup> To date, various materials, such as carbon-based materials,<sup>5–11</sup> conducting polymers<sup>12–14</sup> and transition-metal oxides,<sup>15–18</sup> have been employed as electrodes for supercapacitors. Among these materials, transition metal oxides are considered promising due to their unfilled valence d orbitals (based on the 18 electron rules), which can easily lose electrons and thus achieve multiple accessible valence states to enable a variety of reversible Faraday redox reactions. Furthermore, when two different transition metals are combined, the resulting material exhibits complex chemical compositions and synergistic effect and has high electrochemical activity.

Recently, significant efforts have been made to improve the electrochemical performance of electrode materials by synthesizing transition metal oxides. Tarasankar Pal and his co-workers<sup>19</sup> have described an asymmetric supercapacitor,  $\text{Ni}_3\text{V}_2\text{O}_8\text{@MWCNT}$ , *via* a laboratory-developed modified hydrothermal technique. Ling-Bin Kong and his co-workers<sup>20</sup> have synthesized a hybrid  $\text{Ni}_3\text{V}_2\text{O}_8/\text{Co}_3\text{V}_2\text{O}_8$  nanocomposite by

growing  $\text{Co}_3\text{V}_2\text{O}_8$  nanoparticles on the surface of  $\text{Ni}_3\text{V}_2\text{O}_8$  nanoflakes. H. Chai and his co-workers<sup>21</sup> have reported the quasi-cuboidal  $\text{CoV}_2\text{O}_6$  *via* a microwave-assisted method. Unfortunately, these binary transition metal oxides are either limited by their low electrochemical properties or by technical issues. The complicated synthetic process limits the application of supercapacitors in practical work, and it is necessary to propose a facile and efficient strategy to shorten the material preparation cycle for large-scale production.

In this study, we present a facile chemical co-precipitation process for the synthesis of the high-performance binary transition metal oxide  $\text{CoV}_2\text{O}_6$ . In this process, mild time and energy saving approaches have been developed to achieve the material synthesis. When directly applied as an electrode material,  $\text{CoV}_2\text{O}_6$  exhibited high-capacities ( $306.6 \text{ F g}^{-1}$ ,  $1 \text{ A g}^{-1}$ ;  $219.2 \text{ F g}^{-1}$ ,  $20 \text{ A g}^{-1}$ ) and stable rate capability: after 20 000 cycles, about 83.3% of the capacity was still retained. This strategy opens up a new window for the synthesis of transition metal oxides for application in high-performance supercapacitors.

## Experimental

### Materials

In this study, we used  $\text{CoCl}_2 \cdot 6\text{H}_2\text{O}$  (AR Aladdin Shanghai, China),  $\text{Na}_3\text{VO}_4$  (AR Aladdin Shanghai, China) and KOH (ChengDu KeLong Glass Co. Ltd. ChengDu, China). All the chemicals were of analytical grade and used without any further purification.

### Synthesis of $\text{CoV}_2\text{O}_6$

In a typical procedure, 3 mmol  $\text{CoCl}_2 \cdot 6\text{H}_2\text{O}$  was dissolved in 20 mL deionized water under magnetic stirring at  $70^\circ\text{C}$  for a certain period of time. After this, 2 mmol  $\text{Na}_3\text{VO}_4$  was

State Key Laboratory of Electronic Thin Films and Integrated Devices, School of Electronic Science and Engineering, University of Electronic Science and Technology of China, Chengdu 611731, China. E-mail: cwang@uestc.edu.cn

† Electronic supplementary information (ESI) available. See DOI: 10.1039/c8ra10041a

‡ These authors contributed equally to this work.



dissolved in another 20 mL deionized water under magnetic stirring, and then, this solution was added drop-wise to the cobalt chloride solution. The reaction mixture solution was subsequently stirred vigorously for additional 2 h at 70 °C. After the homogeneous solution was cooled down to room temperature, a brown-red powder precipitate was obtained by washing the homogeneous solution several times with deionized water followed by drying at 60 °C for 12 h in a vacuum oven. Finally, the products were annealed in air at 600 °C for 3 h to obtain  $\text{CoV}_2\text{O}_6$ .

### Characterization

The crystal structure of the products was characterized by X-ray diffraction (XRD), conducted in the range from 10 to 80° using the DX-2700B (Haoyuan) diffractometer with Cu  $K\alpha$  radiation ( $\lambda = 1.5406 \text{ \AA}$ ). The morphology and microstructure of the products were analyzed by scanning electron microscopy (FESEM, JSM-7600F) and transmission electron microscopy (TEM, G2-F30). Moreover, the chemical compositions were examined by XPS measurements *via* ESCALAB 250Xi using Al  $K\alpha$  radiation at 1486.6 eV. The specific surface area and porosity were calculated by the  $\text{N}_2$  adsorption-desorption measurement using the Quadrasorb instrument.

### Electrochemical measurement

All the electrochemical tests were carried out *via* an electrochemical workstation (CHI 660E, CHI Instrument Inc., Shanghai) with a three-electrode electrochemical system in a 3 M KOH aqueous solution. The  $\text{CoV}_2\text{O}_6$ /nickel foam was used as the working electrode, and a platinum plate and Hg/HgO served as the counter and reference electrodes, respectively. The working electrode was prepared by mixing  $\text{CoV}_2\text{O}_6$ , acetylene and poly(vinylidene difluoride) at the mass ratio of 7 : 2 : 1 in a *N*-methyl-2-pyrrolidinone solvent to form a slurry. The slurry was then coated on the one side of the nickel foam (1 cm  $\times$  1 cm) current collectors followed by drying in the vacuum oven at 60 °C for 12 h. Finally, the  $\text{CoV}_2\text{O}_6$ /nickel foam was pressed at 10 MPa, and the mass loading was equal to 1.4 mg. Then, cyclic voltammetry (CV) and galvanostatic charge/discharge (GCD) were performed in the potential window of 0–0.5 V. The specific capacitance was calculated using the following equation:<sup>22</sup>

$$C = \frac{I \Delta t}{m \Delta V}$$

where  $C$  ( $\text{F g}^{-1}$ ) is the specific capacitance,  $I$  (A) is the current density,  $\Delta t$  (s) is the discharge time,  $m$  (g) is the mass of active electrode materials and  $\Delta V$  (V) is the potential window. The frequency range of the electrochemical impedance spectroscopy (EIS) measurements was from  $10^{-2}$  to  $10^5$  Hz.

## Results and discussion

The synthesis process of  $\text{CoV}_2\text{O}_6$  is presented in Fig. 1.  $\text{CoV}_2\text{O}_6$  was prepared by a facile chemical co-precipitation process. The structural features of  $\text{CoV}_2\text{O}_6$  are as follows: it consists of linear

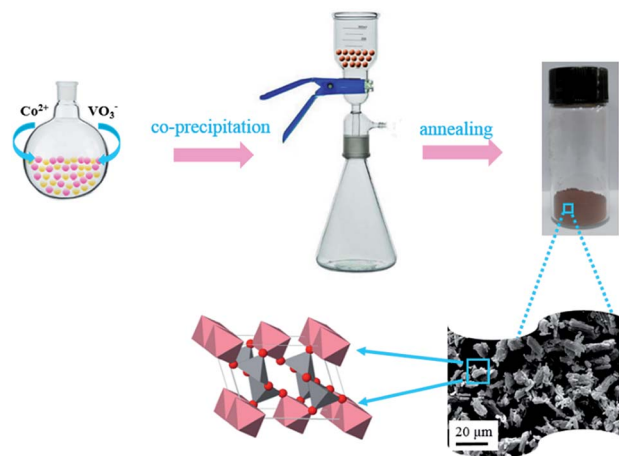
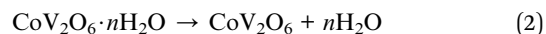
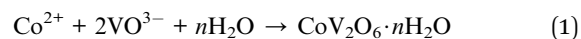


Fig. 1 Schematic of the synthesis of  $\text{CoV}_2\text{O}_6$ . Pink, gray and red represent Co, V, and O, respectively.

chains formed by the  $\text{Co}^{2+}$  ions in the  $\text{CoO}_6$  octahedron as well as zigzag chains formed by the  $\text{V}^{5+}$  ions in  $\text{VO}_5$ . All the chains are along the  $b$ -axis, resulting in a quasi-one-dimensional (1D) structural arrangement ( $a = 9.256 \text{ \AA}$ ,  $b = 3.508 \text{ \AA}$ ,  $c = 6.626 \text{ \AA}$ , and  $\beta = 111.55^\circ$  with the space group  $C2(5)$ ).<sup>23</sup> The chemical reactions can be expressed as follows:



The X-ray diffraction (XRD) patterns of the samples are shown in Fig. 2.  $\text{CoV}_2\text{O}_6 \cdot 4\text{H}_2\text{O}$  (PDF#77-0485) was obtained by the chemical co-precipitation process. After the annealing treatment, high-purity monoclinic  $\text{CoV}_2\text{O}_6$  (PDF#77-1174) was obtained. The annealed samples showed sharp diffraction peaks, which proved the successful synthesis of  $\text{CoV}_2\text{O}_6$  *via* the facile chemical co-precipitation process.

Moreover, X-ray photoelectron spectroscopy (XPS) was used to further confirm the chemical compositions of  $\text{CoV}_2\text{O}_6$ . The

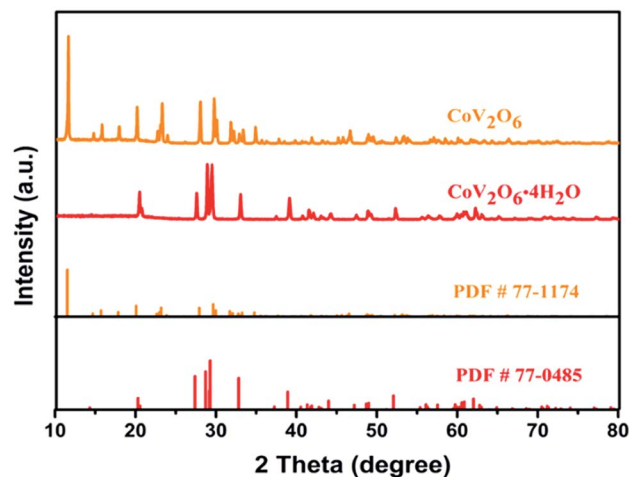


Fig. 2 XRD patterns of  $\text{CoV}_2\text{O}_6 \cdot 4\text{H}_2\text{O}$  and  $\text{CoV}_2\text{O}_6$ .



full spectrum of  $\text{CoV}_2\text{O}_6$  is shown in Fig. S1.† There are two main peaks at 781.47 eV and 797.50 eV in the Co 2p spectrum shown in Fig. S1(b)† due to the spin orbit coupling, corresponding to the hybrid orbitals  $\text{Co } 2p_{3/2}$  and  $\text{Co } 2p_{1/2}$ .<sup>24</sup> The 5d orbitals of the central ions of transition metals become energy degenerate in the imaginary sphere field when subjected to a negative electric field of the ligand. The energy level splitting produces 16.03 eV splitting energy. In addition, two shake-up satellite peaks are observed at 786.18 eV (suggesting that the  $\text{Co}^{2+}$  ions are in an octahedral coordination,<sup>25</sup> matching with the abovementioned structural features) and 803.61 eV, supporting the existence of  $\text{Co}^{2+}$ . Fig. S1(c)† displays the V 2p spectrum of V  $2p_{3/2}$  (516.94 eV) and V  $2p_{1/2}$  (524.19 eV) with a splitting energy of 7.25 eV, indicating that  $\text{V}^{5+}$  also exists. The XPS spectrum of O 1s in Fig. S1(d)† exhibits one typical peak at the binding energy of 530.37 eV assigned to  $\text{O}^{2-}$ .

It has been reported that the specific surface area of the electrode materials plays a crucial role in their electrochemical properties.<sup>26</sup> The results of characterization obtained by the Brunauer–Emmett–Teller (BET) surface analysis are shown in Fig. S2.† Fig. S2(a and b)† display the specific surface areas of  $48.819 \text{ m}^2 \text{ g}^{-1}$  for  $\text{CoV}_2\text{O}_6 \cdot 4\text{H}_2\text{O}$  and  $86.786 \text{ m}^2 \text{ g}^{-1}$  for  $\text{CoV}_2\text{O}_6$ . After the annealing treatment, higher specific surface area is obtained. The pore size distributions show a uniform pore structure, and the pore size of  $\text{CoV}_2\text{O}_6 \cdot 4\text{H}_2\text{O}$  is about 3.6 nm and that of  $\text{CoV}_2\text{O}_6$  is 2.6 nm on the basis of the Barrett–Joyner–Halenda (BJH) analysis results shown in Fig. S2(c and d).† In general, after the annealing treatment, the pore size and the pore volume of the samples decrease; this leads to an increase in the surface area. A larger surface area provides more active sites for ions to participate in the reaction, and thus, a high electrochemical property is obtained.

The surface morphology of  $\text{CoV}_2\text{O}_6$  was characterized by scanning electron microscopy and transmission electron microscopy. Fig. 3(a, b) and S3† show the different magnification SEM images of  $\text{CoV}_2\text{O}_6$ .  $\text{CoV}_2\text{O}_6$  reveals a sponge-like morphology with nanoscale voids constructed by interconnected nanoflakes, and the lengths of the nanoflakes are in the range of 1–5  $\mu\text{m}$ ,<sup>27</sup> which improve the specific surface area and optimize the pore size distribution. Consequently, this provides faster transport channels for ions and electrons in the longitudinal direction; this leads to the internal resistance reduction and electrochemical property increment. Fig. S4† shows an irregular cubic structure with lateral sizes between 1 and 20  $\mu\text{m}$  for  $\text{CoV}_2\text{O}_6 \cdot 4\text{H}_2\text{O}$ .  $\text{CoV}_2\text{O}_6 \cdot 4\text{H}_2\text{O}$  has a smooth surface; however, it agglomerates severely. Furthermore, the morphology of the electrode after cycling is observed by SEM (Fig. S5†). Although a portion of the active materials has collapsed after cycling, the main sponge-like morphology is still retained, and these structures provide sufficient transport channels for the ions and electrons. The TEM images shown in Fig. 3(c and d) indicate that the lattice fringe spacing is approximately 0.2 nm, corresponding to the lattice plane of (003). As observed from the elemental mapping shown in Fig. 3(e), each element is evenly distributed; the more uniform the distribution of the elements, the higher the purity of the samples. An energy dispersive spectrometer (EDS) was

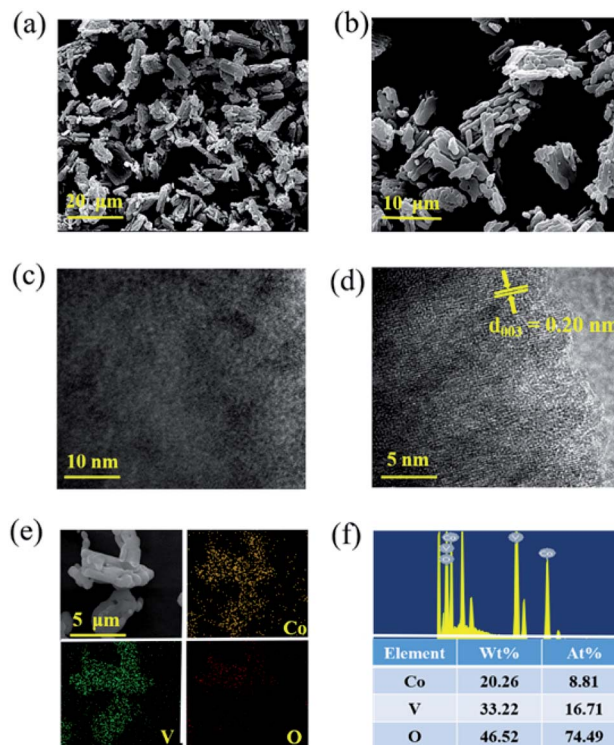
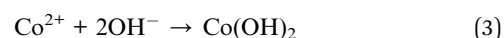


Fig. 3 (a and b) SEM images of  $\text{CoV}_2\text{O}_6$ , (c and d) TEM images of  $\text{CoV}_2\text{O}_6$ , (e) SEM image of  $\text{CoV}_2\text{O}_6$  and its corresponding elemental mapping images: Co, V, and O elements, and (f) the EDS spectrum of  $\text{CoV}_2\text{O}_6$ .

employed to analyse the types and contents of  $\text{CoV}_2\text{O}_6$  and  $\text{CoV}_2\text{O}_6 \cdot 4\text{H}_2\text{O}$ . The results are shown in Fig. 3(f) and S6,† confirming the existence of Co, V, and O. Moreover, the atomic ratio of Co/V is about 1 : 2, which matches well with the chemical formula. To better determine the masses of Co and V, ICP-OES (Inductively coupled plasma optical emission spectrometry) was conducted. The element content of Co and V is 24.6% and 38.1%, respectively. Since cobalt and vanadium are the main components in the sample (more than 10%), the solution needs to be diluted to a large multiple; thus, the result is not the ideal value of 1 : 2 but is approximately 1 : 1.5.

Fig. 4(a) reveals the cyclic voltammetry (CV) curves obtained at the scan rates of 10, 20, 30, 40, and 50  $\text{mV s}^{-1}$  in the potential window of 0–0.5 V. The redox peaks can be clearly observed, indicating that pseudocapacitance plays a dominant role. The cyclic voltammetry curves obtained at different scanning speeds show similar shapes. Generally, these peaks correspond to the reversible reaction of  $\text{Co}^{3+}/\text{Co}^{2+}$  associated with the anions  $\text{OH}^-$ .<sup>1,18,19,28–31</sup> Based on these findings, the reaction mechanism of  $\text{CoV}_2\text{O}_6$  can be presented by following equations:



As the current density increases, the oxidation product and the reduction product migrate to the anode and the cathode, respectively, which are produced during the electrochemical





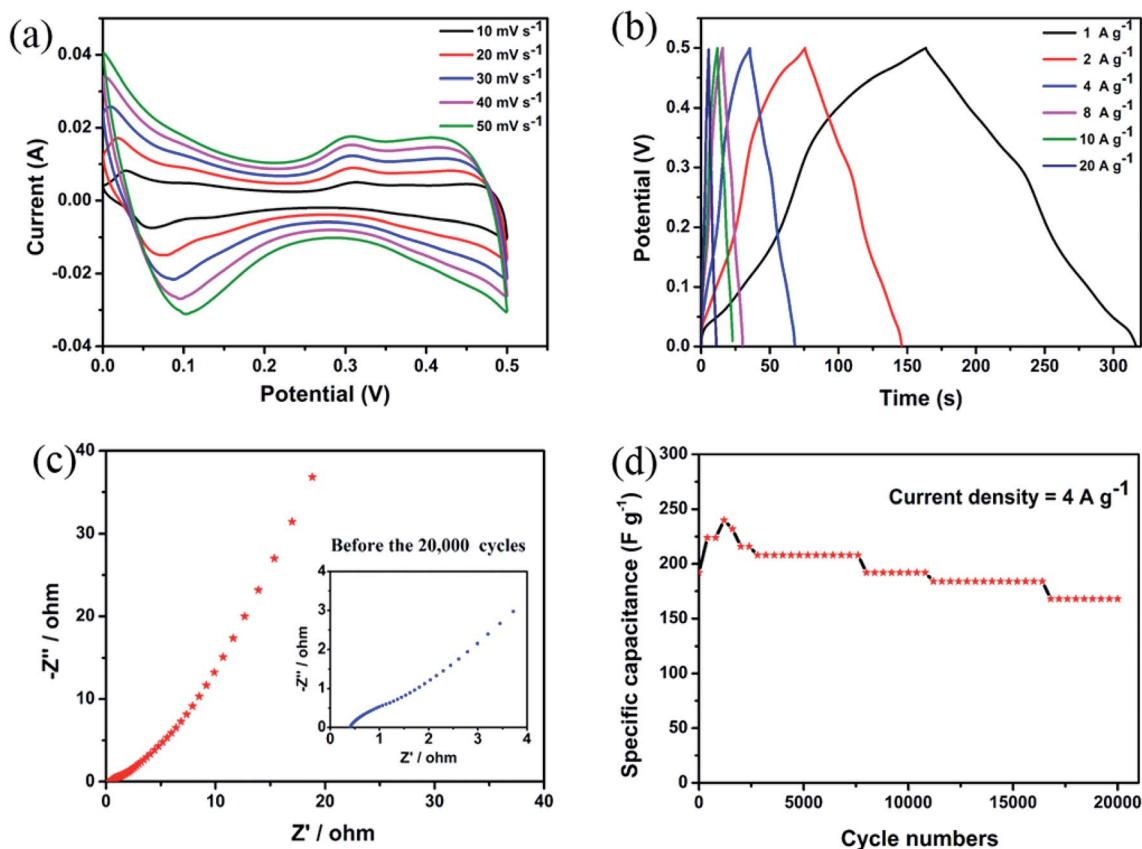


Fig. 4 (a) Cyclic voltammetry (CV) curves of  $\text{CoV}_2\text{O}_6$ . (b) Galvanostatic charge–discharge plots of  $\text{CoV}_2\text{O}_6$ . (c) EIS curves of  $\text{CoV}_2\text{O}_6$  (inset shows the magnified curve). (d) Cycle performance of  $\text{CoV}_2\text{O}_6$ .

reaction due to the irreversible reactions and electric polarization.

To further investigate the electrochemical performance of  $\text{CoV}_2\text{O}_6$ , we tested the galvanostatic charge–discharge (GCD) (Fig. 4(b)) in the potential window of 0–0.5 V. The current density is 1, 2, 4, 8, 10, and 20  $\text{A g}^{-1}$  corresponding to 306.6, 280.8, 261.5, 232.0, 220.0, and 219.2  $\text{F g}^{-1}$ . A detailed comparison is shown in Table S2.† The electrochemical performances of  $\text{CoV}_2\text{O}_6$  synthesized by different methods are quite different, which may be related to their different morphologies. These sponge-like  $\text{CoV}_2\text{O}_6$  have a thinner structure, and they allow more active materials to participate in the Faraday reaction. However, the quasi-cuboidal  $\text{CoV}_2\text{O}_6$  may lock more active substances in the cubic structure. More surprisingly, when the electrode material is subjected to charge and discharge testing at high current density,  $\text{CoV}_2\text{O}_6$  also exhibits a high-capacity (219.2  $\text{F g}^{-1}$ , 20  $\text{A g}^{-1}$ ), which is approximately equal to that of the quasi-cuboidal  $\text{CoV}_2\text{O}_6$  (223  $\text{F g}^{-1}$ , 1  $\text{A g}^{-1}$ ), and a detailed comparison is shown in Table S2.† When the current density increases from 1 to 20  $\text{A g}^{-1}$ , the specific capacitance is still retained at 71.49%; thus, this indicates excellent electrochemical performance of the  $\text{CoV}_2\text{O}_6$  electrode materials for supercapacitors.

In addition, electrochemical impedance spectroscopy (EIS) was used to understand the conductive and diffusive behaviour<sup>32</sup> of  $\text{CoV}_2\text{O}_6$ . The study reveals the EIS in the range from

0.01 Hz to 100 000 Hz with an amplitude of 10 mV. It was carried out before and after continuous charging and discharging for 20 000 cycles, as shown in Fig. 4(c) and S7.† The Nyquist plots show that the  $R_s$  value of  $\text{CoV}_2\text{O}_6$  is 0.47  $\Omega$ ; after cycling, it increases to 0.68  $\Omega$ . The  $R_{ct}$  value before and after cycling are 1.53  $\Omega$  and 0.24  $\Omega$ , respectively. This small change demonstrates that the electrode material has an excellent electrochemical performance.<sup>33</sup>

Note that materials with better cycling stability are more promising in commercial applications. Therefore,  $\text{CoV}_2\text{O}_6$  was tested *via* 20 000 cycles of continuous charge and discharge at the current density of 4  $\text{A g}^{-1}$ . Fig. 4(d) shows that in the first cycle, the specific capacitance of  $\text{CoV}_2\text{O}_6$  is about approximately 192  $\text{F g}^{-1}$ . As the number of cycles increases, the specific capacitance of the electrode shows an upward trend in the first 1200 cycles, then decreases slowly, and after 20 000 cycles, the final retention rate is 83.3%.

## Conclusions

In conclusion, we reported a facile chemical co-precipitation process for the synthesis of the binary transition metal oxide  $\text{CoV}_2\text{O}_6$ .  $\text{CoV}_2\text{O}_6$  demonstrates typical features as follows: (1) high-capacity of 306.6  $\text{F g}^{-1}$  at the current density of 1  $\text{A g}^{-1}$ , and even at the high current density of 20  $\text{A g}^{-1}$ , it still achieves 219.2  $\text{F g}^{-1}$ , (2) stable cycling stability, *i.e.*, 83.3% retention of



the initial value after 20 000 cycles. Accordingly, the superior performance of the CoV<sub>2</sub>O<sub>6</sub> electrode can be attributed to the multiple accessible valence states, which enable fast faradaic reaction. Especially, when two different transition metals are combined, better capacity and cycling stability are achieved. We believe that this study presents an effective method and a new opportunity for promoting the application of electrode materials based on transition metal oxides in supercapacitors.

## Conflicts of interest

There are no conflicts to declare.

## Acknowledgements

This work was supported by the National Natural Science Foundation of China (No. 51672037, 61727818 and 61604031), the subproject of the National Key and Development Program of China (2017YFC0602102), and the Department of Science and Technology of Sichuan Province (No. 2016JQ0022).

## References

- 1 J. Zhang, F. Liu, J. Cheng and X. Zhang, *ACS Appl. Mater. Interfaces*, 2015, **7**, 17630–17640.
- 2 S. Zheng, X. Li, B. Yan, Q. Hu, Y. Xu, X. Xiao, H. Xue and H. Pang, *Adv. Energy Mater.*, 2017, **7**, 1602733.
- 3 Z. Yu, L. Tetard, L. Zhai and J. Thomas, *Energy Environ. Sci.*, 2015, **8**, 702–730.
- 4 Z. Lei, K. Zhao, Y. Luo, Y. Dong, W. Xu, M. Yan, W. Ren, Z. Liang, L. Qu and L. Mai, *ACS Appl. Mater. Interfaces*, 2016, **8**, 7139–7146.
- 5 Z. Tan, G. Chen and Y. Zhu, *Nanocarbons Adv. Energy Storage*, 2015, **1**, 1–489.
- 6 L. L. Zhang and X. Zhao, *Chem. Soc. Rev.*, 2009, **38**, 2520–2531.
- 7 Y. Zhai, Y. Dou, D. Zhao, P. F. Fulvio, R. T. Mayes and S. Dai, *Adv. Mater.*, 2011, **23**, 4828–4850.
- 8 D.-W. Wang, F. Li, J. Zhao, W. Ren, Z.-G. Chen, J. Tan, Z.-S. Wu, I. Gentle, G. Q. Lu and H.-M. Cheng, *ACS Nano*, 2009, **3**, 1745–1752.
- 9 S. Bose, T. Kuila, A. K. Mishra, R. Rajasekar, N. H. Kim and J. H. Lee, *J. Mater. Chem.*, 2012, **22**, 767–784.
- 10 T. Lin, I.-W. Chen, F. Liu, C. Yang, H. Bi, F. Xu and F. Huang, *Science*, 2015, **350**, 1508–1513.
- 11 Y. Li, G. Wang, T. Wei, Z. Fan and P. Yan, *Nano Energy*, 2016, **19**, 165–175.
- 12 G. A. Snook, P. Kao and A. S. Best, *J. Power Sources*, 2011, **196**, 1–12.
- 13 C. Zhou, Y. Zhang, Y. Li and J. Liu, *Nano Lett.*, 2013, **13**, 2078–2085.
- 14 E. Frackowiak, V. Khomenko, K. Jurewicz, K. Lota and F. Béguin, *J. Power Sources*, 2006, **153**, 413–418.
- 15 W. Wei, X. Cui, W. Chen and D. G. Ivey, *Chem. Soc. Rev.*, 2011, **40**, 1697–1721.
- 16 Z. S. Wu, D. W. Wang, W. Ren, J. Zhao, G. Zhou, F. Li and H. M. Cheng, *Adv. Funct. Mater.*, 2010, **20**, 3595–3602.
- 17 T. Y. Wei, C. H. Chen, H. C. Chien, S. Y. Lu and C. C. Hu, *Adv. Mater.*, 2010, **22**, 347–351.
- 18 X. Xia, J. Tu, Y. Zhang, X. Wang, C. Gu, X.-b. Zhao and H. J. Fan, *ACS Nano*, 2012, **6**, 5531–5538.
- 19 R. Sahoo, A. Pal and T. Pal, *J. Mater. Chem. A*, 2016, **4**, 17440–17454.
- 20 M.-C. Liu, L.-B. Kong, L. Kang, X. Li, F. C. Walsh, M. Xing, C. Lu, X.-J. Ma and Y.-C. Luo, *J. Mater. Chem. A*, 2014, **2**, 4919–4926.
- 21 Y. Wang, H. Chai, H. Dong, J. Xu, D. Jia and W. Y. Zhou, *ACS Appl. Mater. Interfaces*, 2016, **8**(40), 27291–27297.
- 22 Z. Li, D. Zhao, C. Xu, J. Ning, Y. Zhong, Z. Zhang, Y. Wang and Y. Hu, *Electrochim. Acta*, 2018, **278**, 33–41.
- 23 Z. He, J. I. Yamaura, Y. Ueda and W. Cheng, *J. Am. Chem. Soc.*, 2009, **131**, 7554–7555.
- 24 V. Soundharrajan, B. Sambandam, J. Song, S. Kim, J. Jo, S. Kim, S. Lee, V. Mathew and J. Kim, *ACS Appl. Mater. Interfaces*, 2016, **8**, 8546–8553.
- 25 B. Sambandam, V. Soundharrajan, V. Mathew, J. Song, S. Kim, J. Jo, D. P. Tung, S. Kim and J. Kim, *J. Mater. Chem. A*, 2016, **4**, 14605–14613.
- 26 J. Hou, C. Cao, F. Idrees and X. Ma, *ACS Nano*, 2015, **9**, 2556–2564.
- 27 Q. Zhou, Y. Gong and J. Lin, *J. Electroanal. Chem.*, 2018, **823**, 80–91.
- 28 Y.-M. Hu, M.-C. Liu, Y.-X. Hu, Q.-Q. Yang, L.-B. Kong, W. Han, J.-J. Li and L. Kang, *Electrochim. Acta*, 2016, **190**, 1041–1049.
- 29 X. Feng, J. Ning, D. Wang, J. Zhang, J. Dong, C. Zhang, X. Shen and Y. Hao, *J. Power Sources*, 2019, **418**, 130–137.
- 30 X. Liu, J. Wang and G. Yang, *ACS Appl. Mater. Interfaces*, 2018, **10**, 20688–20695.
- 31 F. Zhang, C. Yuan, X. Lu, L. Zhang, Q. Che and X. Zhang, *J. Power Sources*, 2012, **203**, 250–256.
- 32 C. Wang, H. Tian, J. Jiang, T. Zhou, Q. Zeng, X. He, P. Huang and Y. Yao, *ACS Appl. Mater. Interfaces*, 2017, **9**, 26038–26044.
- 33 Y. Wang, W. Zhang, X. Guo, K. Jin, Z. Chen, Y. Liu, L. Yin, L. Li, K. Yin and L. Sun, *ACS Appl. Mater. Interfaces*, 2019, **11**, 7946–7953.

